Catalysis Science & Technology

Accepted Manuscript

ROYAL SOCIETY OF CHEMISTRY

www.rsc.org/catalysis

Graphical Abstract

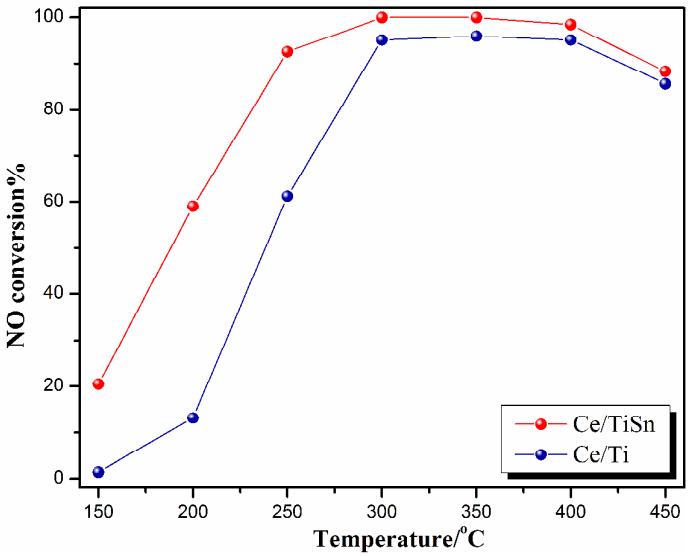

The promotional effect of SnO_2 in Ce/TiO_2 catalyst for NH_3–SCR reaction.

Cite this: DOI: 10.1039/c0xx00000x

ARTICLE TYPE

www.rsc.org/xxxxxx

Promotional effect of doping SnO_2 into TiO_2 over CeO_2/TiO_2 catalyst for the selective catalytic reduction of NO by NH_3

Lei Zhang[a], Lulu Li[a], Yuan Cao[a], Yan Xiong[a], Shiguo Wu[a], Jingfang Sun[b], Changjin Tang[a*], Fei Gao[b], Lin Dong[a,b*]

Received (in XXX, XXX) Xth XXXXXXXXX 20XX, Accepted Xth XXXXXXXXX 20XX
DOI: 10.1039/b000000x

Abstract: $Ti_xSn_{1-x}O_2$ was prepared by co-precipitation method, and a series of $CeO_2/Ti_xSn_{1-x}O_2$ samples were prepared to investigate the effect of doping SnO_2 into TiO_2 for the selective catalytic reduction of NO by NH_3. The results of catalytic tests suggested that the catalyst with the optimal mole ratio (Ti:Sn=1:1) exhibited the best catalytic performances. Moreover, the NO removal efficiency of $CeO_2/Ti_{0.5}Sn_{0.5}O_2$ was higher than that of CeO_2/TiO_2. The obtained samples were characterized by BET, XRD, H_2–TPR, XPS, NH_3–TPD and *in situ* DRIFT. The results revealed that the introduction of SnO_2 resulted in the formation of rutile style $Ti_{0.5}Sn_{0.5}O_2$ solid solution with larger specific surface area and better thermal stability. The interactions between CeO_2 and $Ti_{0.5}Sn_{0.5}O_2$ support could improve the redox performance of catalyst, which was beneficial to enhance catalytic activity at low temperature. Furthermore, doping SnO_2 enhanced surface acid sites and weakened the adsorption of nitrates, which played an important role in the process of catalytic reaction. Finally, *in situ* DRIFT demonstrated that the competition adsorption happened between bridging nitrates and gas NH_3 and the selective catalytic reduction of NO by NH_3 proceeded mainly via the Eley–Rideal mechanism over Ce/TiO_2 and $Ce/Ti_{0.5}Sn_{0.5}O_2$.

1. Introduction

Nitrogen oxides (NO_x) are responsible for acid rain, photochemical smog and ozone depletion threatening ecological environment and human health.[1] Stringent environmental legislation has been made across the world to regulate the emission standard of NO_x from stationary sources (such as coal–fired power plants) and mobile sources (such as vehicle exhaust). The selective catalytic reduction of NO_x by NH_3 (NH_3–SCR) is a kind of high efficient deNO_x technology for the emission reduction of NO_x from coal–fired power plants.[2] The industrial catalysts for NH_3–SCR process are based on TiO_2–supported V_2O_5–WO_3 and/or V_2O_5–MoO_3 oxides for their high NO_x removal efficiency at 300–400 ºC and excellent resistance to SO_2 poisoning. However, V–W(Mo)/TiO_2 catalyst will be gradually replaced for some practical problems: the toxicity of active component V_2O_5, narrow operation temperature window and poor N_2 selectivity at higher temperature.[3–5] In addition, anatase TiO_2 as catalyst carrier is easy to suffer from the crystal transformation to form rutile TiO_2 when temperature is over 600 ºC, which results in the decrease of surface area and catalytic activity.[6, 7]

Nowadays, researches about non–vanadium–SCR catalysts mainly focus on transition metal and rare earth metal catalysts mainly including Fe, Cu, Mn, Ce based catalysts. In addition, the structures and components of catalysts usually influence the NH_3–SCR operation temperature window and the resistance of H_2O and/or SO_2.[7, 8] It is worth noting that CeO_2–TiO_2 based catalysts may be a potential replacement of V_2O_5/WO_3–TiO_2 catalyst for its excellent NO conversion, high N_2 selectivity at medium–high temperature and environmentally–benign characteristic.[9–11]

SnO_2 is a wide band gap n–type semiconducting metal oxide[12, 13] and can form oxygen vacancies,[14, 15] which is widely used in gas sensors, transparent conductors and catalysis. SnO_2 has a rutile–style structure (P42/mnm) as same as rutile TiO_2. It is reported that SnO_2 can be doped into TiO_2 to form rutile $Ti_xSn_{1-x}O_2$ solid solution with high surface area and excellent thermal stability.[16, 17] Meanwhile, our previous studies[18–20] suggest that supported $Ti_{0.5}Sn_{0.5}O_2$ solid solution based catalysts showed excellent NO removal efficiency over both three–way catalysts (TWC) and NH_3–SCR catalysts. Recently, Chang *et.al*[21] reported that adding SnO_2 to MnO_x–CeO_2 could improve the catalytic activity at low temperature and SO_2 resistance in NH_3–SCR reaction.

In this work, we attempt to substitute $Ti_{0.5}Sn_{0.5}O_2$ solid solution for TiO_2 over CeO_2/TiO_2 to prepare $CeO_2/Ti_{0.5}Sn_{0.5}O_2$ by an impregnation method. Catalytic performance evaluation suggests that $CeO_2/Ti_{0.5}Sn_{0.5}O_2$ displayed higher NO removal rate than

CeO_2/TiO_2 within the whole temperature range. Therefore, we focus on investigating the promotional effect of doping SnO_2 into TiO_2 on NH_3–SCR performances over CeO_2/TiO_2. To elucidate the functions of $Ti_{0.5}Sn_{0.5}O_2$ in NH_3–SCR reaction, textural structure, surface acidity, redox performance and surface component of samples have been explored by BET, XRD, *in situ* DRIFT, H_2–TPR, NH_3–TPD and XPS.

2. Experimental

2.1. Catalyst preparation

A series of $Ti_xSn_{1-x}O_2$ solid solution (x is molar ratio) were prepared by a co-precipitation method. An ethanol and water mixed solution containing required amounts of $TiCl_4$ and $SnCl_4$ was precipitated by ammonium hydroxide under vigorous stirring (pH ≈ 9.0). The precipitate was washed with deionized water until no Cl^- could be detected by 1.0 $mol \cdot L^{-1}$ $AgNO_3$ solution, then dried at 110 ºC for 12 h and calcined at 550 ºC for 4 h in flowing air.

Both anatase TiO_2 (denoted as TiO_2–A) and rutile TiO_2 (denoted as TiO_2–R) were prepared by $TiCl_4$ dropwise into ethanol in an ice-water bath under stirring. The differences were that TiO_2–A was obtained by adding appropriate amount of $NH_3 \cdot H_2O$ until the pH value was 9.0 while TiO_2–R was obtained by adding appropriate amount of H_2O (pH < 1.0). Furthermore, SnO_2 was prepared by the same procedure as anatase TiO_2 and $SnCl_4$ was used as the precursor. The precipitate was washed with distilled water to be free of chloride, then dried at 110 ºC for 12 h and calcined at 500 ºC for 4 h in flowing air.

A series of $y CeO_2/Ti_xSn_{1-x}O_2$ (denoted as yCe/Ti_xSn_{1-x}, and "y" is the mass fraction of CeO_2 in sample) and CeO_2/TiO_2 (using anatase TiO_2 as support, denoted as Ce/Ti) were prepared by incipient wetness impregnation with the solution of $Ce(NO_3)_3 \cdot 6H_2O$. The samples were vigorously stirred for 1 h and then evaporated at 100 ºC until achieving a paste, which was dried at 110 ºC overnight and then calcined in a muffle stove at 500 ºC for 4 h in flowing air. For yCe/$Ti_{0.5}Sn_{0.5}$, the CeO_2 loading was 5%, 10%, 15% and 20 *wt.*% respectively. For Ce/Ti and Ce/Sn samples, the CeO_2 loading was fixed at 10 *wt.*%.

2.2. Catalyst characterization

X-ray powder diffraction (XRD) patterns were collected using a Philips X'pert Pro diffractometer with Ni-filtered CuKα1 radiation (0.15408 nm). The X–ray tube was operated at 40 kV and 40 mA. Average crystallite size was calculated by Debye–Scherrer equation.[22]

Specific surface areas of samples were measured by nitrogen adsorption at 77 K on a Micrometrics ASAP–2020 analyzer by the Brunauer–Emmet–Teller (BET) method. Before each adsorption measurement, about 0.1 g of the sample was degassed in a N_2/He mixture at 300 ºC for 4 h.

X–ray photoelectron spectroscopy (XPS) experiments were performed on a PHI 5000 Versa Probe high performance electron spectrometer, using monochromatic Al Kα radiation (1486.6 eV) operating at an accelerating power of 15 kW. Before the measurement, the sample was outgassed at room temperature in a UHV chamber (< 5×10^{-7} Pa). The sample charging effects were compensated by calibrating all binding energies (BE) with the adventitious C 1s peak at 284.6 eV. This reference gave BE values with accuracy at ± 0.1 eV.

H_2–temperature programmed reduction (H_2–TPR) was carried out in a quartz U–tube reactor connected to a TCD with H_2–Ar mixture (7% H_2 by volume) as reductant. 50 mg of the sample was used for each measurement. Before switching to the H_2–Ar stream, the sample was pre-treated in a N_2 stream at 200 ºC for 1 h. TPR started from room temperature to 850 ºC at a rate of 10 $ºC \cdot min^{-1}$.

The *in situ* DRIFT experiments were performed on a Nicolet Nexus 5700 FTIR spectrometer by using a diffuse reflectance attachment (HARRICK) equipped with a reaction cell (ZnSe windows). The number of scans was 32 at a resolution of 4 cm^{-1} and the spectra were presented as Kubelka-Munk function referred to background spectra of sample recorded in N_2. The powder sample was used (*ca.* 25 mg) and pre-treated in N_2 at 400 ºC for 1 h prior to adsorption experiments. The reaction conditions as follows: 500 ppm NH_3, 500ppm NO, 5 vol.% O_2, N_2 balance and 100 $ml \cdot min^{-1}$ flow rate. For each sample, the NH_3/(NO + O_2) were adsorbed for 45 min to steady state at required temperature. Afterwards, (1) the sample was purged by N_2 for 10 min, then spectra were recorded in pure N_2 stream at a desired temperature by the heating rate of 10 $ºC \cdot min^{-1}$; (2) the sample was purged by N_2 for 10 min, then passing (NO + O_2)/NH_3 into the gas chamber to react with the pre–adsorbed NH_3/NO_x species.

NH_3–temperature programmed desorption (NH_3–TPD) experiments were carried out on a multifunction chemisorption analyzer with a quartz U–tube reactor, detected by a thermal conductivity detector (TCD). About 0.1 g of the sample was pre–treated by high purified N_2 (40 $ml \cdot min^{-1}$) at 450 ºC for 1 h. After pre–treatment, the sample was saturated with 1 vol.% NH_3 (10 $ml \cdot min^{-1}$) at 100 ºC for 1 h and subsequently flushed with high purified N_2 at the same temperature for 1 h to remove gaseous and weakly adsorbed NH_3, then the sample was heated to 600 ºC at a rate of 10 $ºC \cdot min^{-1}$ in the flowing high purified N_2 (40 $ml \cdot min^{-1}$).

2.3. Catalytic performance test

Catalytic reaction was performed in a fixed–bed quartz reactor tube. The reaction condition were: 500 ppm NO, 500 ppm NH_3, 5 vol.% O_2, 100 ppm SO_2 (when used), 5 vol.% H_2O (when used), balance N_2 and the gas flow rate of 100$ml \cdot min^{-1}$, GHSV was 90,000 h^{-1}. Prior to catalytic test, the sample was pre–treated in N_2 at 200 ºC for 1 h. The effluent gases including NO, NH_3, NO_2, and N_2O were continuously analysed by an online Nicolet IS10 spectrometer equipped with a gas cell. IR Data were collected at required temperature with keeping reaction for 15 min to reach a steady state. The NO conversion and N_2 selectivity were calculated by the following equations:

$$\text{NO conversion } (\%) = \frac{[NO]_{in} - [NO]_{out}}{[NO]_{in}} \times 100$$

N_2 selectivity (%)

$$= \frac{[NO]_{in} - [NO]_{out} + [NH_3]_{in} - [NH_3]_{out} - [NO_2]_{out} - 2[N_2O]_{out}}{[NO]_{in} - [NO]_{out} + [NH_3]_{in} - [NH_3]_{out}} \times 100$$

3. Results and discussion

3.1. Catalytic performances evaluation

3.1.1. Effect of doping SnO_2 on catalytic activity over Ce/Ti

Firstly, the influence of Ti/Sn mole ratio on NO conversion over Ce/Ti_xSn_{1-x} samples was investigated. Herein, the loading of CeO_2 was fixed at 10 wt.%. As shown in Fig. S1, the order of catalytic activity followed $Ce/Ti_{0.5}Sn_{0.5}$ > $Ce/Ti_{0.75}Sn_{0.25}$ > $Ce/Ti_{0.9}Sn_{0.1}$ > $Ce/Ti_{0.95}Sn_{0.05}$ > $Ce/Ti_{0.25}Sn_{0.75}$. The results of catalytic activities indicated that Ce/Ti_xSn_{1-x} samples exhibited the optimal NO conversion when the molar ratio of Ti/Sn was 1:1. So a series of $y Ce/Ti_{0.5}Sn_{0.5}$ samples were prepared, and comparative studies between $Ce/Ti_{0.5}Sn_{0.5}$ (Ce/TiSn for short) and Ce/Ti samples were conducted to elucidate the effect of doping SnO_2 on NH_3–SCR performances.

Fig. 1 showed the NO conversion as a function of temperature for NH_3–SCR over Ce/TiSn, Ce/Ti, Ce/Sn, TiSn support and CeO_2. It could be seen that Ce/Sn, TiSn solid solution and CeO_2 exhibited much poor catalytic activity. In contrast, Ce/Ti displayed better catalytic activity with over 90% NO conversion between 300 ºC and 400 ºC while Ce/TiSn samples had the best catalytic activity with more than 88% NO conversion from 250 ºC to 450 ºC in the present experimental conditions. The order of catalytic activity followed Ce/TiSn > Ce/Ti > Ce/Sn > CeO_2> TiSn, indicating the sample with triple components had the best catalytic activity. Based on the above results, doping SnO_2 into TiO_2 was beneficial to improve the catalytic activity of Ce/Ti, and the promotional effect was possible related to the interactions among CeO_2, SnO_2 and TiO_2. It is worth noting that the loading amounts of CeO_2 for Ce/TiSn had little effect on catalytic activity. Thus, it is rational to choose the 10Ce/TiSn sample as a represent to investigate the promotional effect of SnO_2 on CeO_2/TiO_2. Fig. S2 indicated that the N_2 selectivity of Ce/TiSn and Ce/Ti was more than 95% in the entire temperatures. In addition, as shown in Fig.S3, when 10Ce/TiSn was calcined at 750 ºC for 4 h, although the catalytic activity of 10Ce/TiSn decreased, its catalytic activity was much higher than that of Ce/Ti calcined at 750 ºC, which indicated that Ce/TiSn had better thermal stability than Ce/Ti.

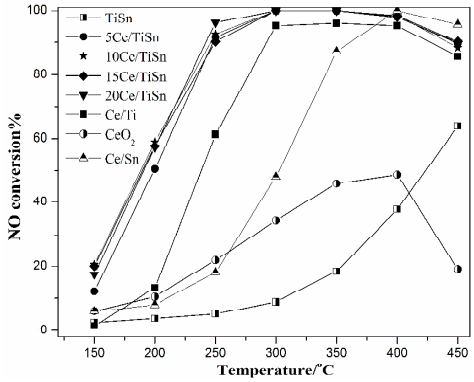

Fig. 1 NO conversion of CeO_2, TiSn, Ce/Sn, Ce/Ti, and Ce/TiSn samples.

3.1.2. NO + O_2 reaction on 10Ce/TiSn and Ce/Ti

As reported elsewhere,[23–26] the oxidation of NO to NO_2 over catalysts (such as V_2O_5–WO_3/TiO_2 and Fe–zeolite catalysts) could improve the low temperature NH_3–SCR activity by the "fast SCR" reaction route as following:

$NO + NO_2 + 2NH_3 \rightarrow 2N_2 + 3H_2O$

In order to investigate the influence of doping SnO_2 on NH_3–SCR catalytic activities at low temperature, NO oxidation reaction was conducted in the range from 150 to 450 ºC. As shown in Fig. 2, the NO conversion of 10Ce/TiSn was higher than that of Ce/Ti at the same reaction temperature. It seemed that NH_3–SCR proceeded more easily via the "fast SCR" reaction route over 10Ce/TiSn. Possible reasons for improving the "fast SCR" reaction by doping SnO_2 would be discussed combined with the results of XPS and H_2–TPR.

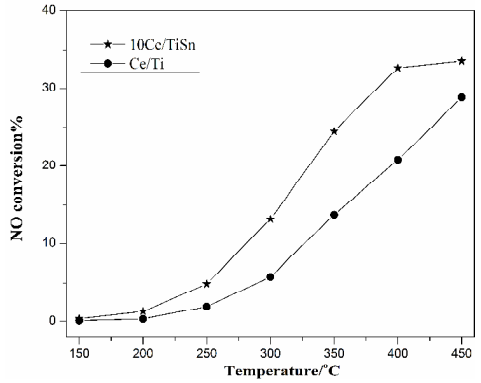

Fig. 2 NO conversion in NO oxidation over Ce/Ti and 10Ce/TiSn. Reaction conditions: 500 ppm NO and 5 vol.% O_2.

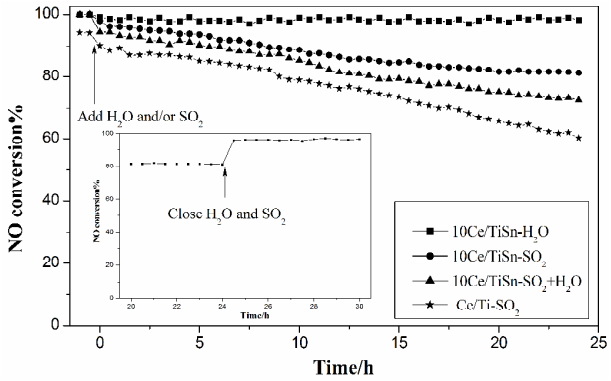

Fig. 3 5 vol.% H_2O and/or 100 ppm SO_2 resistance testing over Ce/Ti and 10Ce/TiSn.

3.1.3. Effect of H_2O and/or SO_2 on catalytic activity over 10Ce/TiSn and Ce/Ti

The actual working conditions of coal fired plants usually contained a certain amount of SO_2 and H_2O, thus it was necessary to investigate the influence of SO_2 and H_2O on SCR activities of catalysts.[27] All tests were carried out at 300 ºC. As shown in Fig. 3, 5 vol.% H_2O had basically no influence on the activity of 10Ce/TiSn with keeping nearly 100% NO conversion in the whole testing. When 100 ppm SO_2 was injected, the NO conversion of 10Ce/TiSn slowly decreased with the increase of time and maintained ca. 81% after 24 h. Meanwhile, NH_3–SCR in the presence of 100 ppm SO_2 was measured over Ce/Ti as a comparison, and NO conversion decreased from ca. 94% to ca. 62% after 24 h. Thus, it indicated that doping SnO_2 into TiO_2 could improve the SO_2 resistance of Ce/Ti. When both SO_2 and H_2O were introduced, the NO conversion of 10Ce/TiSn was lower than that of only adding SO_2 in the whole testing. In terms of the accelerated deactivation of catalyst influenced by H_2O, two possible reasons could be proposed. On one hand, NH_4HSO_4 could be more easily formed in the presence of SO_2 and H_2O than only introducing SO_2, which led to the deactivation of catalysts.[28]

On the other hand, active sites could be occupied by the adsorbed H_2O as a consequence of the competitive adsorption of NH_3 and H_2O, which resulted in the reversible deactivation of catalysts.[29] Thus, catalysts were easier to be deactivated by introducing both SO_2 and H_2O comparing to only introducing SO_2. Interestingly, it could be seen that NO conversion could recover up to ca. 96% when cutting off SO_2 and H_2O over 10Ce/TiSn (the inset in Fig. 3), which indicated that the deactivation in the coexistence of SO_2 and H_2O was reversible over Ce/TiSn. As reported elsewhere,[30, 31] the NH_3–SCR activity could be regenerated automatically after cutting off SO_2 and H_2O over $Ce_{0.2}W_{0.2}TiO_x$ or Fe–Mn/TiO_2 catalysts.

3.2. Structural characterization (XRD and BET)

As shown in Fig. S4, Ti_xSn_{1-x} (x=0–1) samples were rutile–style structure (PDF 77–0450 for pure SnO_2 and PDF 78–1510 for pure TiO_2). With the increase of Ti/Sn mole ratio, diffraction peak gradually shifted to lower angle (the effective ionic radius $r(Sn^{4+})$ = 0.069 nm > $r(Ti^{4+})$ = 0.0605 nm) comparing to TiO_2–R, indicating that Sn^{4+} had been successfully incorporated into the lattice of TiO_2 to form TiSn solid solution maintaining the rutile–style structure, which was in agreement with the literatures.[16, 22, 32] When CeO_2 was supported and the loading amount of CeO_2 was less than 10 *wt.*%, as shown in Fig. 4, only the peaks related to TiSn support were detected, which indicated that CeO_2 was dispersed on the surface of TiSn support or its particle size was smaller than the detection limit of XRD. When CeO_2 loading was more than 15 *wt.*%, the peaks at 28.6° and 47.6° ascribed to CeO_2 phase were emerged. Combined with the results of catalytic activity, it could be seen that crystalline CeO_2 over Ce/TiSn catalyst had little effect on catalytic performance. In addition, diffraction peaks of TiSn became significantly broader than those of pure TiO_2 and SnO_2, indicating the smaller size of crystallite for TiSn as summarized in Table 1. Meanwhile, the specific surface area of TiSn solid solution was much larger than those of pure TiO_2 and SnO_2, which suggested that the introduction of SnO_2 improved the textural structure of TiO_2.

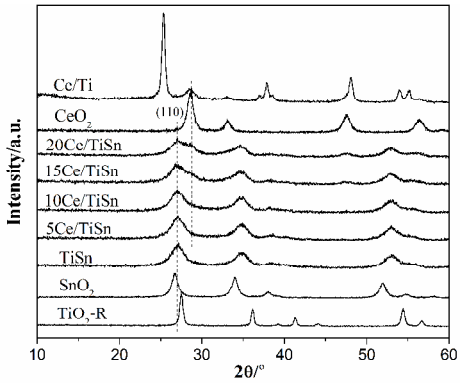

Fig. 4 XRD results of supports and catalysts.

3.3. Surface component and chemical states (XPS)

XPS was performed to illustrate the surface component and chemical state of elements in Ce/Ti and 10Ce/TiSn samples. The CeO_2 spectrum was composed of two multiplets (v and u) by Gaussian–Lorentz fitting procedure with the assignment defined in Fig. 5 of Ce 3d spectra. The bands labelled u stand for $3d_{3/2}$ spin–orbit states and those labelled v represented $3d_{5/2}$ states. The bands labelled as u' and v' were ascribed to the primary photoemission of Ce^{3+} and the other six bands labelled as u''' and v''', u'' and v'', u and v were assigned to Ce^{4+}.[33] Ce^{3+} content could be estimated by the formula:[34]

$$Ce(III)\% = \frac{100\times\left[S(u')+S(v')\right]}{\Sigma\left[S(u)+S(v)\right]}\%$$

Table 1 The textural data of supports and catalysts.

Sample	BET surface area/$m^2\cdot g^{-1}$	Crystallite size/nm	a=b /nm	c/nm
TiO_2–A	54.2	22.6	-	-
TiO_2–R	19.5	33.9	0.4602	0.2972
SnO_2	30.5	22.3	0.4692	0.3151
$Ti_{0.5}Sn_{0.5}O_2$	86.4	10.2	0.4640	0.3058
10Ce/TiSn	75.6	-	-	-
Ce/Ti	47.3	-	-	-

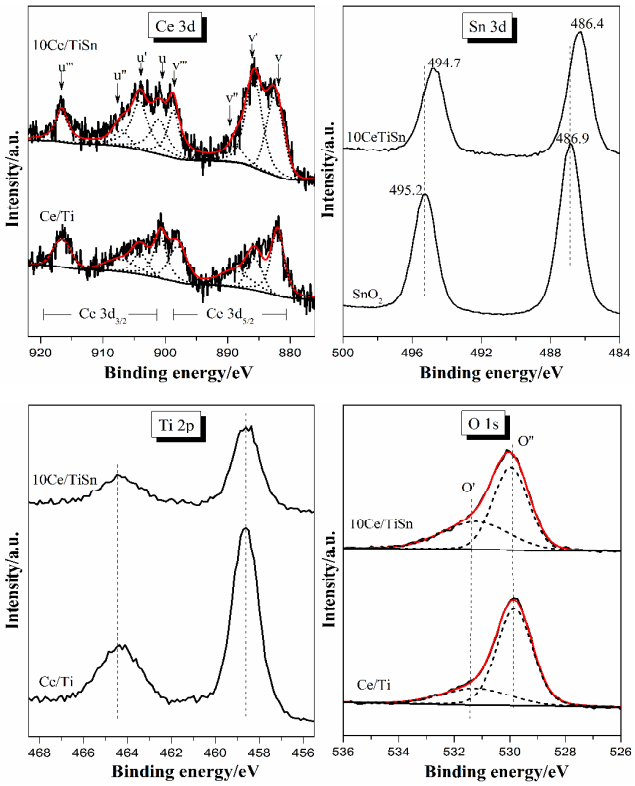

Fig. 5 XPS spectra of Ce 3d, Sn 3d, Ti 2p, O 1s for Ce/Ti and 10Ce/TiSn.

As listed in Table 2, the relative content of Ce^{3+} increased from 17.0% in Ce/Ti to 35.1% in 10Ce/TiSn. Meanwhile, in terms of Sn 3d, it can be seen that the bands of 10Ce/TiSn shifted to lower binding energy comparing to these of pure SnO_2, indicating that part of low valence tin species existed over 10Ce/TiSn sample. However, the binding energies of Ti 2p for Ce/Ti and 10Ce/TiSn samples kept unchanged. Thus, the increase of Ce^{3+} over 10Ce/TiSn sample could be due to the synergetic interaction of CeO_2 and SnO_2 via the redox equilibrium of $2Ce^{4+} + Sn^{2+} \leftrightarrow 2Ce^{3+} + Sn^{4+}$, as reported by the previous studies.[35, 36] In

addition, For the XPS spectra of O1s, the band of O' at 531.2 eV could be assigned to surface adsorbed oxygen species and the band of O" at 529.8 eV could be ascribed to lattice oxygen.[37] From data listed in Table 2, the relative content of O' over 10Ce/TiSn was larger than that of Ce/Ti sample, which indicated that more surface adsorbed oxygen species were formed over 10Ce/TiSn sample. Therefore, in NH_3–SCR reaction, the synergetic interaction between CeO_2 and SnO_2 was beneficial to activate O_2 molecular to react with NO, which could improve the "fast–SCR" route over Ce/TiSn.

3.4. Redox performances (H_2–TPR)

In NH_3–SCR reaction, the reaction temperature window of NO removal rate largely depended on the redox properties of catalyst. Therefore, the influence of doping SnO_2 on the reducibility performance of Ce/Ti was investigated by H_2–TPR. As shown in Fig. 6, pure CeO_2 displayed two peaks at ca. 500 and 780 ºC, which could be respectively assigned to surface oxygen and bulk lattice oxygen reduction.[38–40] In terms of pure SnO_2, a strong reduction peak located at 630 ºC could be ascribed to the reduction of Sn^{4+} to metal Sn.[35, 41] In addition, TiSn solid solution displayed the similar redox behaviour as pure SnO_2. The peak α of Ce/Ti could be ascribed to the dispersed CeO_2, and peak β was due to the reduction of bulk TiO_2.[42, 43] With regard to Ce/TiSn, peak α (150–500 ºC) could be ascribed to the reduction of surface species including Ce^{4+} or/and Sn^{4+} and peak β (above 500 ºC) could be due to the reduction of bulk species including bulk TiSn and CeO_2. Compared with Ce/Ti and TiSn samples, peaks α and β of Ce/TiSn samples shifted to the lower temperature, it could be explained that the interaction between CeO_2 and SnO_2 evidenced by XPS could improve the redox properties of Ce/TiSn. Considering the results of NO + O_2 reaction, it could be deduced that the better redox properties of Ce/TiSn promoted the occurrence of "fast–SCR" reaction and enhanced the NO removal rate at low temperature over Ce/TiSn.

Table 2 The fitting data of XPS over Ce/Ti and 10Ce/TiSn.

Sample	$Ce^{3+}/(Ce^{3+}+Ce^{4+})$/%	O'/(O' +O")/%
Ce/Ti	17.0	23.9
10Ce/TiSn	35.1	39.5

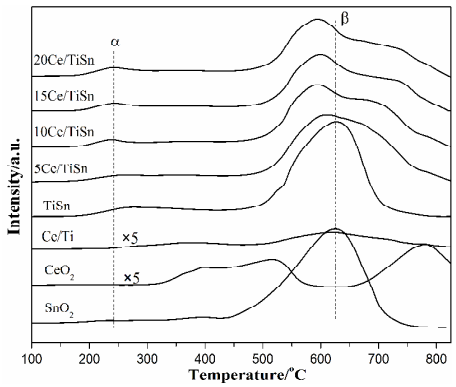

Fig. 6 H_2–TPR results of supports and catalysts.

3.5. Surface molecular adsorption (*in situ* DRIFT)

3.5.1. NH_3 adsorption–desorption

In order to investigate the differences of NH_3 adsorption behaviours over the samples induced by doping SnO_2, the DRIFT spectra of NH_3 adsorption–desorption were recorded from 150 to 350 ºC. NH_3 adsorption results of pure TiO_2 and TiSn solid solution were respectively shown in Fig. 7a and 7b. The triplet peaks in the range of 3100-3400 cm^{-1} could be assigned to the N–H stretching vibration of coordinated NH_3, the peaks in the range of 1660–1680 cm^{-1} and 1490–1450 cm^{-1} could be ascribed to ionic NH_4^+ bounded to Brønsted acid sites (denoted as B acids), and the peaks in the range of 1610–1580 cm^{-1} and 1160–1220 cm^{-1} could be assigned to the coordinated NH_3 bounded to Lewis acid sites (denoted as L acids).[44, 45] It could be seen that B acids totally desorbed after the temperature exceeded 300 ºC and L acids still exhibited even at 350 ºC, which indicated that L acid sites were stronger acid sites than B acid sites over Ce/Ti and 10Ce/TiSn. Compared with pure TiO_2, the peaks of L acids at 1160–1220 cm^{-1} obviously were widened in the range from 1100 cm^{-1} to 1300 cm^{-1} and the intensity of B acids at 1490–1450 cm^{-1} increased over TiSn solid solution. It was reported that peak of L acid appeared at about 1240–1250 cm^{-1} for pure SnO_2[46] and Shen *et.al*[47] also found that a new peak of L acid at 1195 cm^{-1} appeared for NH_3 adsorption over SnO_2/Al_2O_3 compared with pure Al_2O_3. Thus, L acid sites consisted of not only NH_3 bounded to TiO_2 at *ca.* 1180 cm^{-1} but also NH_3 bounded to SnO_2 at *ca.* 1220 cm^{-1} over Ce/TiSn. It could be seen that doping SnO_2 into TiO_2 could enhance the sort and amount of acid sites over TiO_2. As shown in Fig. 7c and 7d, Ce/Ti and 10Ce/TiSn respectively exhibited a similar spectrum as the corresponding support. By carefully comparing to pure supports, the peaks of NH_3 adsorption over Ce/Ti and 10Ce/TiSn shifted to higher wavenumbers, implying that the adsorption behaviour of NH_3 was influenced probably by the interaction between CeO_2 and supports.

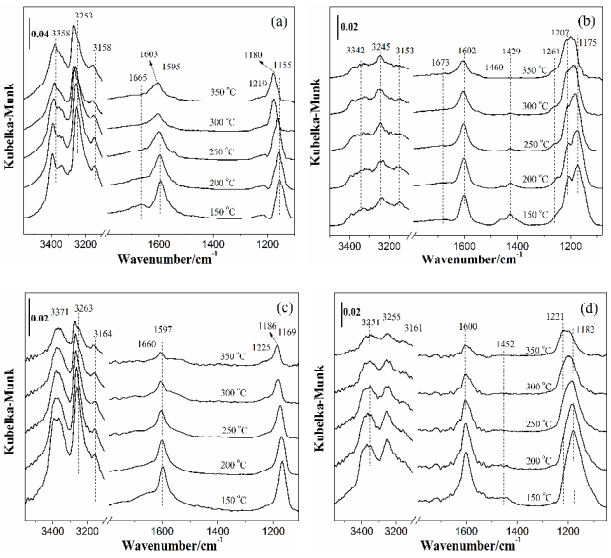

Fig. 7 *In situ* DRIFT spectra of NH_3 adsorption–desorption over TiO_2 (a), TiSn (b), Ce/Ti (c) and 10Ce/TiSn (d).

3.5.2. NO + O_2 adsorption–desorption

NO + O_2 adsorption–desorption spectra were recorded from 150 to 400 ºC to investigate the adsorption differences of nitrogen oxides between Ce/Ti and 10Ce/TiSn samples. It was reported

that IR active modes of nitrates adsorbed on metal oxides are located in 1650–1500 cm^{-1} and 1300–1200 cm^{-1}.[48] As shown in Fig. 8a for Ce/Ti sample, different kinds of surface nitrate species formed during the process of NO + O_2 desorption. According to the change regulation of peak intensity and precious studies, the peaks at 1616, 1579 and 1230 cm^{-1} could be attributed to bridging nitrates (including bridging monodentate and bridging bidentate nitrates as shown in Fig. S5), the peaks at 1554 and 1245 cm^{-1} could be ascribed to chelating bidentate nitrates, the peaks at 1510 and 1286 cm^{-1} could be assigned to monodentate nitrates, and the peak at 1351 cm^{-1} could be due to free nitrate ions.[48] Raising the temperature from 150 to 400 ºC, the intensity of monodentate nitrates continuously decreased and totally eliminated at 350 ºC. Similarly, the peaks of bidentate nitrates also decreased but still existed at 400 ºC. However, the intensity of bridging nitrates increased firstly and then decreased. All the results indicate that the transformation from monodentate nitrates to bridging nitrates occurred during the process of thermal desorption, and the order of thermal stability for these nitrate species followed bridging nitrates > bidentate nitrates > monodentate nitrates. In terms of 10Ce/TiSn sample shown in Fig. 8b, the peaks at 1612, 1575 and 1232 cm^{-1}, 1545 and 1250 cm^{-1}, 1510 and 1280 cm^{-1} could be respectively assigned to bridging nitrates, chelating bidentate nitrates and monodentate nitrates. The intensity of all peaks uniformly decreased with the increase of temperature and completely disappeared at 400 ºC, which indicated that nitrate species over 10Ce/TiSn were continuously desorbing and the desorption of nitrate species over 10Ce/TiSn was easier than that of Ce/Ti. Our previous study suggested that the adsorption of NO_x species on the surface of SnO_2 was considerably weak.[35] Based on the present results, it could be seen that doping SnO_2 resulted in weakening the adsorption ability of nitrate species over Ce/TiSn.

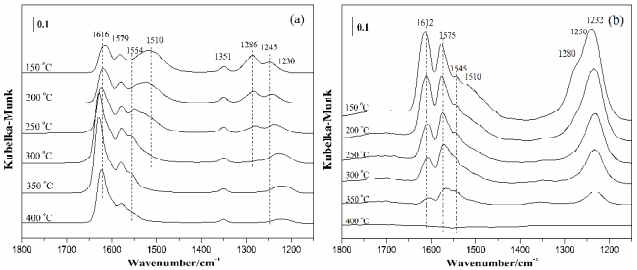

Fig. 8 *In situ* DRIFT spectra of NO + O_2 adsorption–desorption over Ce/Ti (a) and 10Ce/TiSn (b).

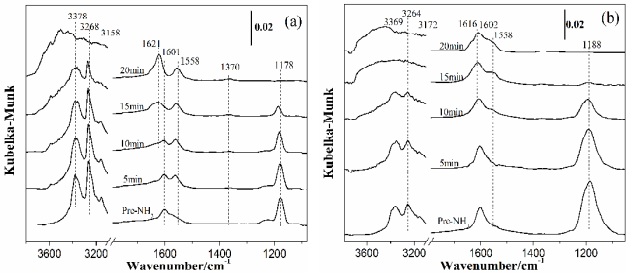

Fig. 9 *In situ* DRIFT spectra of NO + O_2 reaction with pre–adsorbed NH_3 over Ce/Ti (a) and 10Ce/TiSn (b) at 250 ºC.

3.5.3. NO + O_2 adsorption after pre–adsorption NH_3

NH_3 was pre–adsorbed over Ce/Ti and 10Ce/TiSn samples for 1 h followed by N_2 purging, and then NO and O_2 were introduced and the DRIFT spectra were collected as a function of time. The results of Ce/Ti sample were shown in Fig. 9a. The peaks at 1601 and 1178 cm^{-1} due to L acids and the peaks of N–H stretching vibration in the range of 3100–3400 cm^{-1} decreased with the increase of time and disappeared after 20 min. With the consumption of adsorbed NH_3, the peak at 1621 cm^{-1} due to bridging nitrates and 1558 cm^{-1} due to bidentate nitrates appeared. It implied that NH_3 coordinated with L acid sites was the active species and the reaction between pre–adsorption NH_3 and NO + O_2 proceeded by Eley–Rideal (E–R) mechanism. As shown in Fig. 9b, the adsorption behaviours of 10Ce/TiSn were similar to those of Ce/Ti sample. The peaks of L acids at 1602 and 1188 cm^{-1} gradually disappeared accompanying with the appearance of nitrate species, which indicates that E–R mechanism could proceed over 10Ce/TiSn sample. As reported elsewhere,[44, 49] NH_3–SCR process mainly followed E–R mechanism over tungsten or manganese modified Ce/TiO_2 based catalysts, and the reaction between adsorbed NH_3 species and NO gas was a key intermediate reaction. In addition, it is worth noting that the peaks of N–H stretching vibration in 3100–3400 cm^{-1} and the peak at 1188 cm^{-1} due to L acid mostly disappeared after 15min, and the consumption rate of NH_3 over 10Ce/TiSn was faster than that of Ce/Ti, indicating that doping SnO_2 into TiO_2 promoted the activation of NH_3.

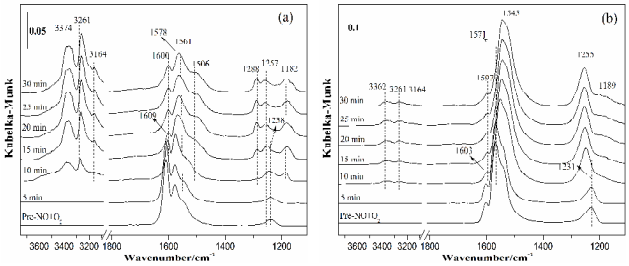

Fig. 10 *In situ* DRIFT spectra of NH_3 reaction with pre–adsorbed NO + O_2 over Ce/Ti (a) and 10Ce/TiSn (b) at 250 ºC.

3.5.4. NH_3 adsorption after pre–adsorption NO + O_2

NO and O_2 were pre–adsorbed over Ce/Ti and 10Ce/TiSn samples for 1 h followed by N_2 purging, NH_3 was introduced and the DRIFT spectra were recorded as a function of time. In terms of Ce/Ti shown in Fig. 10a, bridging nitrates at 1609, 1578 and 1238 cm^{-1} and chelating bidentate nitrates at 1561 and 1257 cm^{-1} formed. After injecting NH_3 for 10 min, L acids at 1600 and 1182 cm^{-1} formed with N–H stretching peaks in the range of 3100–3400 cm^{-1}. In the meantime, the peaks at 1506 and 1288 cm^{-1} due to monodentate nitrates formed and the intensity of bidentate nitrates at 1561 and 1257 cm^{-1} increased with the intensity of bridging nitrates at 1609, 1578 and 1238 cm^{-1} decreasing. NO + O_2 adsorption–desorption has demonstrated that the order of thermal stability followed bridging nitrates > bidentate nitrates > monodentate nitrates over Ce/Ti sample. Therefore, the possibility that the disappearance of bridging nitrates was caused by thermal desorption could be ruled out. In addition, surface adsorption was saturated over the samples for 1 h NO+O_2 pre-adsorption judged from the DRIFT intensity of nitrate species. Thus, it could be deduced that competition adsorption happened between bridging nitrates and gas NH_3. Combined with DRIFT results, it could be proposed that one NH_3 molecular could snatch

an adsorption site from bridging nitrates to form one L acid, and then bridging nitrates transformed to monodentate and chelating bidentate nitrates over Ce/Ti as shown in Fig. S5. With regard to 10Ce/TiSn (in Fig. 10b), NH_3 adsorption resulted in the disappearance of bridging nitrates at 1603, 1571 and 1231 cm^{-1} after 10 min. Meanwhile the broad and asymmetric peaks at 1545 and 1255 cm^{-1} including in monodentate and chelating bidentate nitrates increased. Thus, it could be seen that competition adsorption as shown in Fig. S5 also happened over 10Ce/TiSn sample. It was worth noting that the competition adsorption over Ce/Ti and 10Ce/TiSn was beneficial to form L acids, which guaranteed the successful proceeding of NH_3–SCR reaction by E–R mechanism. After injecting NH_3 for 10 min, although L acids at 1597 and 1189 cm^{-1} formed, the intensities of both nitrate species and NH_3 bounded to L acids kept unchanged over Ce/Ti and 10Ce/TiSn samples, indicating the adsorbed nitrate species could not react with the adsorbed NH_3 species. Therefore, NH_3–SCR reaction could not proceed by Langmuir–Hinshelwood (H–L) mechanism over Ce/Ti and 10Ce/TiSn.

From the above results of *in situ* DRIFT, doping SnO_2 influenced the adsorption behaviors of both ammonia and nitrate species. Comparing to Ce/Ti sample, the adsorption behaviors over Ce/TiSn sample were characterized as following: 1. increasing the sorts of L acid sites; 2. weakening the adsorption of nitrates; 3. improving the activation of NH_3. *In situ* DRIFT results demonstrated that NH_3–SCR reaction proceeded by E–R mechanism over the studied samples, since the adsorption of nitrate species was weakened over Ce/TiSn by doping SnO_2, L acid sites were not easily blocked by nitrate species and could be highly effective to activate NH_3.

Table 3 The amount of surface acids over supports and catalysts.

Sample	Weak acids S_α/a.u.	Strong acids S_β/a.u.	Total acids S_α+ S_β/a.u.
TiO_2–A	6630	14038	20668
TiSn	7889	20224	28113
Ce/Ti	3756	9885	13461
10Ce/TiSn	5922	14597	20519

3.6. Surface acidities (NH_3–TPD)

NH_3–TPD was carried out to further investigate the effect of doping SnO_2 on acid properties over the samples. As shown in Fig. 11, all the TPD curves could be fitted into peak α and peak β indicating two different kinds of acid species. NH_3 adsorption DRIFT had displayed that B acids totally desorbed at 300 ºC and L acids still exhibited even at 350 ºC, thus peak α for weak acid could be ascribed to B acid and peak β for strong acid could be assigned to L acid. As listed in Table 3, the amount of L acid was higher than that of B acid for all the samples. Meanwhile, the total acid amount of TiSn solid solution was larger than that of pure TiO_2, which indicated that surface acid sites of TiO_2 were added by doping SnO_2 due to the increase of specific surface area and the new added acid sites on SnO_2. When loading CeO_2 on TiO_2 and TiSn solid solution, the total acid amount of Ce/Ti and Ce/TiSn decreased compared with pure supports because of the decrease of specific surface area**.** Thus, NH_3–TPD results indicated that doping SnO_2 into TiO_2 could enhance the amount of acid sites over Ce/Ti sample.

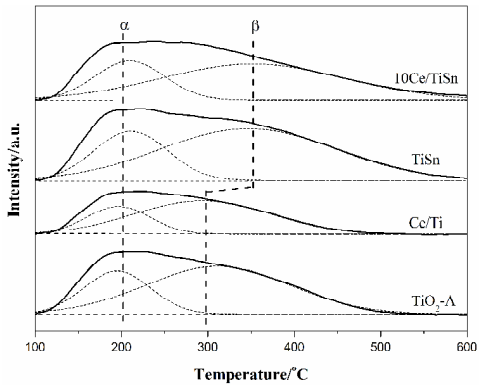

Fig. 11 NH_3–TPD results of supports and catalysts.

4. Conclusions

Based on the all above results and discussion, Ce/TiSn sample exhibited better catalytic performances than Ce/Ti sample by doping SnO_2 into TiO_2, the reasons as following:

1. Rutile $Ti_{0.5}Sn_{0.5}O_2$ solid solution prepared by co–precipitation method displayed more excellent texture structure than pure anatase or rutile TiO_2, including larger specific surface area and better thermal stability in NH_3–SCR reaction.

2. H_2–TPR and XPS suggested that doping SnO_2 into TiO_2 improved the redox ability of Ce/TiO_2 and enhanced the interaction between CeO_2 and TiSn support, which contributed to the "fast–SCR" route and promoted the deNO_x activity at low temperature.

3. *In situ* DRIFT results suggested that competition adsorption happened between bridging nitrates and gas NH_3 and NH_3–SCR reaction proceeded by the Eley–Rideal mechanism over Ce/Ti and Ce/TiSn. Doping SnO_2 not only improved L acid sites to activate NH_3 but also weakened the adsorption ability of nitrates, which was conductive to push forward NH_3–SCR reaction by Eley–Rideal mechanism. In addition, NH_3–TPD demonstrated that the amount of acid sites increased by doping SnO_2.

Acknowledgements

The financial supports of the National Natural Science Foundation of China (Nos. 21303082, 21273110), Doctoral Fund of Ministry of Education of China (No. 2013009111005) and Sinopec Shanghai Research Institute of Petrochemical Technology are gratefully acknowledged.

Notes and references

[a]*Key Laboratory of Mesoscopic Chemistry of MOE, School of Chemistry and Chemical Engineering, Nanjing University, Nanjing, 210093, P. R. China*

[b]*Jiangsu Key Laboratory of Vehicle Emissions Control, Center of Modern Analysis, Nanjing University, Nanjing 210093, PR China*

Corresponding author:

Fax: +86 25 83317761; Phone: +86 25 83592290

Address: Hankou Road 22#, Nanjing, Jiangsu province, P. R. China, 210093

E-mail address: donglin@nju.edu.cn (L. Dong); tangcj@nju.edu.cn (C. J. Tang)

1 G. Liu and P.-X. Gao, *Catal. Sci. Technol.*, 2011, 1, 552–568.
2 M. F. Fu, C. Li, P. Lu, L. Qu, M. Y. Zhang, Y. Zhou, M. G. Yu and Y. Fang, *Catal. Sci. Technol.*, 2014, 4, 14–25.
3 G. Buscaa, L. Liettib, G. Ramisa and F. Berti, *Appl. Catal. B: Environ.*, 1998, 18, 1–36.
4 P. Forzatti, *Appl. Catal. A: Gen.*, 2001, 222 221–236.
5 P. G. Smirniotis, D. A. Pena and B. S. Uphade, *Angew. Chem. Int. Ed.*, 2001, 40, 2479–2481.
6 M. Suzana, P. Francisco and V. R. Mastelaro, *Chem. Mater.*, 2002, 14, 2514–2518.
7 F. D. Liu, Y. B. Yu and H. He, *Chem. Commun.*, 2014, 50, 8445–8463.
8 F. D. Liu, W. P. Shan, X. Y. Shi, C. B. Zhang and H. He, *Chin. J. Catal.*, 2011, 32, 1113–1128.
9 X. Gao, Y. Jiang, Y. Zhong, Z. Y. Luo and K. F. Cen, *J. Hazard. Mater.*, 2010, 174, 734–739.
10 W. P. Shan, F. D. Liu, H. He, X. Y. Shi and C. B. Zhang, *ChemCatChem*, 2011, 3, 1286–1289.
11 X. Gao, Y. Jiang, Y. C. Fu, Y. Zhong, Z. Y. Luo and K. F. Cen, *Catal. Commun.*, 2010, 11, 465–469.
12 Y. Wang, X. Jiang and Y. Xia, *J. Am. Chem. Soc.*, 2003, 125, 16176–16177.
13 K. Zakrzewska, *Thin Solid Films*, 2001, 391, 229–238.
14 M. EpifaniJoan, D. Prades, E. Comini, E. Pellicer, M. Avella, P. Siciliano, G. Faglia, A. Cirera, R. Scotti, F. Morazzoni and J. R. Morante, *J. Phys. Chem. C*, 2008, 112, 19540–19546.
15 L. Z. Liu, T. H. Li, X. L. Wu, J. C. Shen and P. K. Chu, *J. Raman Spectrosc.*, 2012, 43, 1423–1426.
16 S. K. Kulshreshtha, R. Sasikala and V. Sudarsan, *J. Mater. Chem.*, 2001, 11, 930–935.
17 H. Uchiyama and H. Imai, *Chem. Commun.*, 2005, 6014–6016.
18 L. H. Dong, L. L. Zhang, C. Z. Sun, W. J. Yu, J. Zhu, L. J. Liu, B. Liu, Y. H. Hu, F. Gao, L. Dong and Y. Chen, *ACS Catal.*, 2011, 468–480.
19 C. Sun, L. Dong, W. Yu, L. Liu, H. Li, F. Gao, L. Dong and Y. Chen, *J. Mol. Catal. A: Chem.*, 2011, 346, 29–38.
20 L. H. Dong, B. Zhang, C. J. Tang, B. Li, L. Y. Zhou, F. Z. Gong, B. Z. Sun, F. Gao, L. Dong and Y. Chen, *Catal. Sci. Technol.*, 2014, 4, 482–493.
21 H. Z. Chang, X. Y. Chen, J. H. Li, L. Ma, C. Z. Wang, C. X. Liu, J. W. Schwank and J. M. Hao, *Environ. Sci. Technol.*, 2013, 47, 5294–5301.
22 E. W. McFarland and H. Metiu, *Chem. Rev.*, 2013, 113, 4391─4427.
23 C. Ciardelli, I. Nova, E. Tronconi, D. Chatterjee and B. Bandl–Konrad, *Chem. Commun.*, 2004, 2718–2719.
24 E. Tronconi, I. Nova, C. Ciardelli, D. Chatterjee and M. Weibel, *J. Catal.*, 2007, 245, 1–10.
25 A. Grossale, I. Nova, E. Tronconi, D. Chatterjee and M. Weibel, *J. Catal.*, 2008, 256, 312–322.
26 A. Grossale, I. Nova and E. Tronconi, *J. Catal.*, 2009, 265, 141–147.
27 R. K. Srivastava, C. A. Miller, C. Erickson and R. Jambhekar, *J. Air Waste Manage.*, 2004, 54, 750-762.
28 Z. G. Huang, Z. P. Zhu and Z. Y. Liu, *Appl. Catal. B: Environ.*, 2002, 39, 361–368.
29 C.-H. Lin and H. Bai, *Ind. Eng. Chem. Res.*, 2004, 43, 5983-5988.
30 W. Shan, F. Liu, H. He, X. Shi and C. Zhang, *Appl. Catal. B: Environ.*, 2012, 115–116, 100–106.
31 G. Qi and R. T. Yang, *Appl. Catal. B: Environ.*, 2003, 44, 217–225.
32 X. Z. Ding, Z. A. Qi and Y. Z. He, *NanoStruct. Mater.*, 1994, 4, 663–668.
33 S. Watanabe, X. L. Ma and C. S. Song, *J. Phys. Chem. C*, 2009, 113, 14249–14257.
34 A. J. Silvestre, R. F. Rodríguez and E. A. Sepúlveda, *J. Catal.*, 2002, 210, 127–136.
35 X. J. Yao, Y. Xiong, W. X. Zou, L. Zhang, S. G. Wu, X. Dong, F. Gao, Y. Deng, C. J. Tang, Z. Chen, L. Dong and Y. Chen, *Appl. Catal. B: Environ.*, 2014, 144, 152–165.
36 T. Baidya, A. Gupta, P. A, Deshpandey, G. Madras and M. S. Hegde, *J. Phys. Chem. C*, 2009, 113, 4059–4068.
37 D. R. Sellick, A. Aranda, T. García, J. M. López, B. Solsona, A. M. Mastral, D. J. Morgan, A. F. Carley and S. H. Taylor, *Appl. Catal. B: Environ.*, 2013, 132–133, 98–106.
38 M. J. Sun, G. J. Zou, S. Xu and X. L. Wang, *Mater. Chem. Phys.*, 2012, 134, 912–920.
39 W. Miśta, M. A. Małecka and L. Kępiński, *Appl. Catal. A: Gen.*, 2009, 368, 71–78.
40 R. Qu, X. Gao, K. Cen and J. Li, *Appl. Catal. B: Environ.*, 2013, 142–143, 290–297.
41 X. J. Yao, C. J. Tang, Z. Y. Ji, Y. Dai, Y. Cao, F. Gao, L. Dong and Y. Chen, *Catal. Sci. Technol.*, 2013, 3, 688–698.
42 P. R. Ettireddy, N. Ettireddy, S. Mamedov, P. Boolchand and P. G. Smirniotis, *Appl. Catal. B: Environ.*, 2007, 76, 123–134.
43 S. Watanabe, X. L. Ma and C. S. Song, *J. Phys. Chem. C*, 2009, 113, 14249–14257.
44 L. Chen, J. H. Li and M. G. Fa, *Environ. Sci. Technol.*, 2010, 44, 9590–9596.
45 D. Wang, L. Zhang, K. Kamasamudram and W. S. Epling, *ACS Catal.*, 2013, 3, 871–881.
46 P. G. Harrisona and E. W. Thornton, *J. Chem. Soc. Faraday Trans.*, 1975, 71, 1013–1020.
47 J. Y. Shen, R. D. Cortright, Y. Chen and J. A. Dumesic, *Catal. Lett.*, 1994, 26, 247–257.
48 K. I. Hadjiivanov, *Catal. Rev.*, 2000, 42, 71–144.
49 Z. B. Wu, B. Q. Jiang, Y. Liu, H. Q. Wang and B. R. Jin, *Environ. Sci. Technol.*, 2007, 41, 5812–5817.